Combinatorial Growth and Anisotropy Control of Self-Assembled Epitaxial Ultrathin Alloy Nanowires

Francisco Javier Bonilla,[†] Anastasiia Novikova,[‡] Franck Vidal,[†,*] Yunlin Zheng,[†] Emiliano Fonda,[‡] Dominique Demaille,[†] Vivien Schuler,[†] Alessandro Coati,[‡] Alina Vlad,[‡] Yves Garreau,[‡,§] Michèle Sauvage Simkin,[‡] Yves Dumont,[⊥] Sarah Hidki,[†] and Victor Etgens[†,∥]

[†]Institut des NanoSciences de Paris, CNRS UMR 7588, UPMC Université Paris 06, 4 Place Jussieu, 75005 Paris, France, [‡]Synchrotron Soleil, L'Orme des Merisiers Saint-Aubin BP 48, 91192 Gif-sur-Yvette Cedex, France, [§]Université Paris Diderot, Sorbonne Paris Cité, MPQ, UMR 7162 CNRS, Bâtiment Condorcet, Case Courrier 7021, 75205 Paris Cedex 13, France, [⊥]Groupe d'Etude de la Matière Condensée (GEMaC), CNRS-UVSQ, 45 Avenue des Etats-Unis, 78035 Versailles Cedex, France, and [∥]Université de Versailles Saint-Quentin en Yvelines 55, Av. de Paris, 78035 Versailles, France

ABSTRACT Self-assembled vertical epitaxial nanostructures form a new class of heterostructured materials that has emerged in recent years. Interestingly, such kind of architectures can be grown using combinatorial processes, implying sequential deposition of distinct materials. Although opening many perspectives, this combinatorial nature has not been fully exploited yet. This work demonstrates that the combinatorial character of the growth can be further exploited in order to obtain alloy nanowires coherently embedded in a matrix. This issue is illustrated in the case of a fully epitaxial system: Co_xNi_{1-x} nanowires in $CeO_2/SrTiO_3(001)$. The advantage brought by the ability to grow alloys is illustrated by the control of the magnetic anisotropy of the nanowires when passing from pure Ni wires to Co_xNi_{1-x} alloys. Further exploitation of this combinatorial approach may pave the way toward full three-dimensional heteroepitaxial architectures through axial structuring of the wires.

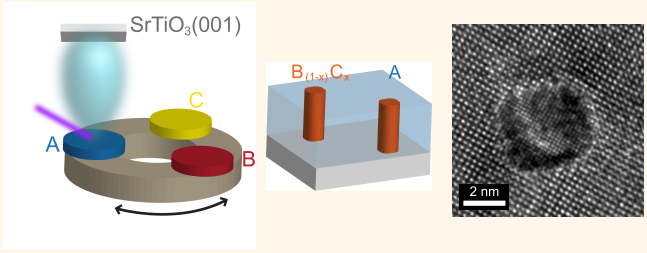

KEYWORDS: self-assembly · heteroepitaxy · nanowires · CoNi alloys · magnetic anisotropy

Heteroepitaxy of planar "horizontal" structures is a well-established way to obtain coherent stacks of distinct materials, resulting in monolithic devices used for applications in many areas, from optoelectronics to spintronics. In comparison, the field of vertical heterostructures growth is still in its infancy, although tremendous progress has been achieved recently.[1] Indeed, the last five years or so have seen an increasing interest in the growth of self-assembled vertical heteroepitaxial nanostructures made of a matrix of material A hosting embedded nanocolumns of material B, with A and B epitaxied.[2−10]

Among the main motivations for growing such structures, one can cite the following issues: (i) due to the geometry, interfacial coupling of the physical properties of material A and B may be enhanced, for example, such effect could give rise to artificial multiferroics;[2,4,8−10] (ii) vertical heteroepitaxy may be exploited in a strain-engineering approach, in order to tune a strain-dependent physical property of the nanocomposite;[6] (iii) vertical heteroepitaxy is a promising way to obtain ferromagnetic nanowires assemblies that may find applications in data storage device.[3,11]

These appealing perspectives motivate efforts to improve the growth procedures. Among recent progress, one can cite the lateral ordering by using patterned substrates and the use of combinatorial schemes, *i.e.*, growth process involving sequential deposition of compounds, the sequence being adjusted in order to reach the desired composition and structure. Indeed, in a seminal paper by Fruchart *et al.* on self-organized Co nanopillars on Au(111), such combinatorial schemes, involving sequential deposition of Co and Au, were already proposed.[12] More recent studies deal with nanocomposite systems grown by pulsed laser deposition (PLD). Originally, most compounds were grown starting from a single

* Address correspondence to vidal@insp.jussieu.fr.

Received for review January 3, 2013 and accepted April 19, 2013.

Published online April 29, 2013
10.1021/nn4000308

target, containing a mix of matrix and pillar materials, as the source material.[2−8] However, PLD allows one to use combinatorial schemes implying sequential deposition of the compounds forming the pillars and the matrix, down to the submonolayer regime. Such an approach has been used recently to grow $CoFe_2O_4$ nanopillars embedded in a $BaTiO_3$ matrix[10] and $CoFe_2O_4$ nanopillars embedded in a $SrRuO_3$ matrix.[13]

In the present work, we go one step further in the exploitation of the combinatorial nature of the growth process and demonstrate the possibility to grow embedded alloy nanowires. The combinatorial approach is illustrated in Figure 1. Starting from targets of materials A, B, C (Figure 1a), it is possible to adjust the growth sequence in order to deposit the desired amount of each material and to obtain self-assembled wires made of a $B_{1-x}C_x$ alloy embedded in an epitaxial matrix made of material A, Figure 1b. Using a nucleation and growth picture, the self-assembly can be understood as illustrated in Figure 1c: after deposition of A, submonolayer deposition of B leads to cluster nucleation and growth on the surface of A; further deposition of A leads to burial of B; deposition of C will lead to nucleation and growth at the apex of B; then deposition of A ends the sequence that can be repeated in order to grow the structure depicted in Figure 1b. In this paper, we demonstrate the feasibility of such an approach by growing embedded epitaxial Co_xNi_{1-x} alloy nanowires. Furthermore, we illustrate the advantages of the technique in order to tune a physical property of the obtained nanocomposite, in the present case, the magnetic anisotropy of the system.

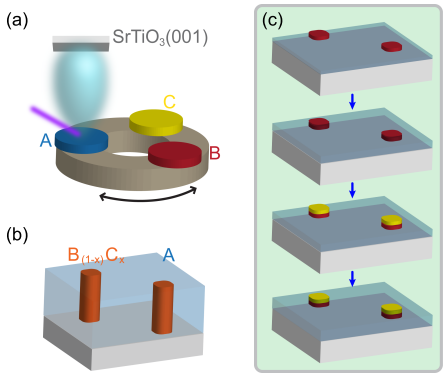

Figure 1. (a) Schematic illustration of the combinatorial growth of self-assembled epitaxial nanocomposites. (b) Sequential pulsed laser deposition on three targets made of materials A, B and C allows one to produce $B_{1-x}C_x$ vertical epitaxial nanostructures coherently embedded in a matrix made of material A. (c) Illustration of the nucleation and growth processes leading to the formation of the structure depicted in panel b.

RESULTS AND DISCUSSION

In previous studies, we have shown that it is possible to grow Co wires with diameters of a few nanometers in $CeO_2/SrTiO_3(001)$ epilayers by PLD.[14−17] The structure of such Co wires is complicated by the hcp−fcc phase transition of Co. Contrary to Co, Ni crystallizes in the fcc structure only, with a lattice parameter a_{Ni} = 3.524 Å. The lattice parameter of CeO_2 (cubic fluorite structure) is a_{CeO_2} = 5.411 Å. As $2a_{CeO_2} \simeq 3a_{Ni}$, epitaxy between Ni and CeO_2 may be favored.

We thus start this section by evidencing the formation of epitaxial Ni nanowires in CeO_2 epilayers grown on $SrTiO_3(001)$, our starting point for the growth of Co_xNi_{1-x} alloy nanowires. Figure 2a,b shows typical energy-filtered transmission electron microscopy (EFTEM) images acquired at the Ni L-edge in plane view and cross section geometry of a Ni containing CeO_2 epilayer using the procedure described in the Methods section. These EFTEM images provide a chemical mapping of Ni location and allow us to evidence the formation of nanowires-like regions with a high Ni concentration, oriented with their long axis along the growth direction, [001], and with diameters of the

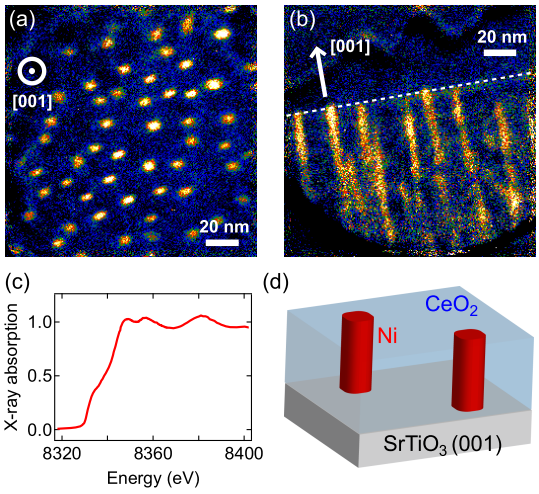

Figure 2. (a and b) EFTEM images, taken at the Ni L-edge, of a Ni containing CeO_2 film grown on $SrTiO_3(001)$. The arrow indicates the growth direction along [001] of $SrTiO_3$. (c) XANES spectrum at the Ni K-edge of a Ni containing CeO_2 film grown on $SrTiO_3(001)$. (d) Schematic illustration of the structure of the sample.

order of 4.5 nm. To complement such local analysis and to probe the chemical state of Ni in the whole sample, X-ray absorption spectroscopy was carried out at the Ni K-edge. The spectrum in Figure 2c is characteristic of metallic Ni. Thus, EFTEM and X-ray absorption data combined together reveal the formation of metallic Ni nanowires as illustrated in Figure 2d.

Cross-sectional imaging of a Ni rich region detected in EFTEM mode using high resolution transmission electron microscopy (HRTEM) reveals the existence of narrow regions, elongated in the [001] direction where the matrix pattern is disturbed, as shown in Figure 3a. The Fourier transform of the HRTEM image depicted in Figure 3a is shown in Figure 3b with the diffraction spots indexed. The spots of the CeO_2 matrix are highlighted by blue circles and those of Ni by red squares.

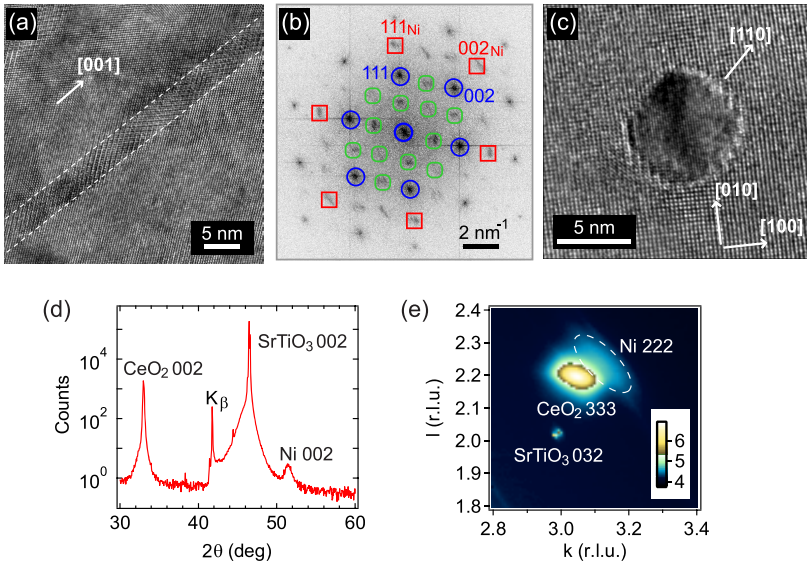

Figure 3. (a) High resolution TEM cross section of an epitaxial Ni nanowire in $CeO_2/SrTiO_3(001)$; zone axis $[1\bar{1}0]CeO_2$. (b) Fourier transform of panel a with indexed spots. (c) High resolution TEM plane view of an epitaxial Ni nanowire in $CeO_2/SrTiO_3(001)$. (d) $\theta-2\theta$ scan of a Ni nanowires assembly embedded in $CeO_2/SrTiO_3(001)$. (e) Reciprocal space mapping of a Ni nanowires assembly embedded in $CeO_2/SrTiO_3(001)$. r.l.u. stands for reciprocal lattice unit.

All other spots (light green) can be deduced from the Ni and CeO_2 spots and indexed by considering multiple diffraction events arising in cross-sectional geometry. The Ni spots are aligned with those of the matrix, indicating a cube-on-cube epitaxy of Ni and CeO_2. Such an epitaxial relationship is also evident in HRTEM images acquired in plane view, see Figure 3c. To confirm the epitaxy, evidenced by local TEM measurements, X-ray diffraction measurements were carried out. Figure 3d shows a $\theta-2\theta$ scan of the sample confirming the alignment of $[001]_{Ni}$ and $[001]_{CeO_2}$. The full epitaxial relationships were confirmed by reciprocal space mapping, such as the one in Figure 3e indicating that $[111]_{Ni}$ and $[111]_{CeO_2}$ are parallel, and ϕ-scans (not shown).

It is thus possible to grow epitaxial Ni nanowires embedded in $CeO_2/SrTiO_3(001)$ epilayers. Starting from this system, we use the combinatorial approach and growth sequences indicated in the Methods section in order to test the possibility of growing Co_xNi_{1-x} alloy nanowires with adjusted values of x. Such tuning of x is achieved through the control of the Ni/Co nominal ratio (ratio of laser shots on the targets). From spectroscopic analysis of the Co and Ni content in the samples (see Methods), a Ni/Co nominal ratio of 0.5 led to $Co_{0.63}Ni_{0.37}$ and a nominal ratio of 2 led to $Co_{0.32}Ni_{0.68}$. These compositions are quite close to those expected from the ratio of laser shots on the targets. This shows that the growth method allows us to tune the composition of the alloys by adjusting the growth sequence.

Figure 4a,b shows EFTEM plane views at the Ni and Co L-edges of a sample grown with a Ni/Co nominal ratio of 2, leading to $Co_{0.32}Ni_{0.68}$. In both images, disks indicating a high Co or Ni concentration are clearly resolved. These disks, having diameters of the order of 4.5 nm, correspond to the section of the nanowires. The digital difference of these two chemical maps is shown in Figure 4c. The overall uniformity of this difference image shows that the disks corresponding to a high Ni concentration and the ones corresponding to a high Co concentration are superimposed. This provides clear evidence that Co *and* Ni are present in the same nanowire. The fcc structure and cube-on-cube epitaxy are preserved, as evidenced by the typical HRTEM plane view and cross section in Figure 4d–f. The metallic state of the wires was then confirmed by X-ray absorption spectroscopy at the Co K-edge and at the Ni K-edge, see Figure 5. Moreover, Co K-edge XANES spectra differ from that of pure hcp-Co and mimic that of fcc-Ni. The separation and relative weight of the peaks labeled A and B confirm that the alloy wires crystallize in the fcc structure.[18−20]

The fact that the wires are made from alloys and not from alternated Ni and Co sections is warranted by the choice of growth sequence and growth temperature. From the final thickness of the CeO_2 epilayer, it is straightforward to deduce the mean amount of material added at the apex of the wires during a sequence. The mean increase in wire length during a sequence is of the order of 1 Å. Thus, it is straightforward to consider that the nanowires grow as an alloy and not a sequence of distinct Co and Ni staking layers.

From TEM plane view measurements, the mean diameter and the density of the alloy nanowires assemblies could be measured. We get a diameter of 4.5 ± 0.2 nm and a density of $(1.16 \pm 0.03) \times 10^{12}$ in.$^{-2}$. We note that such density compares favorably with the

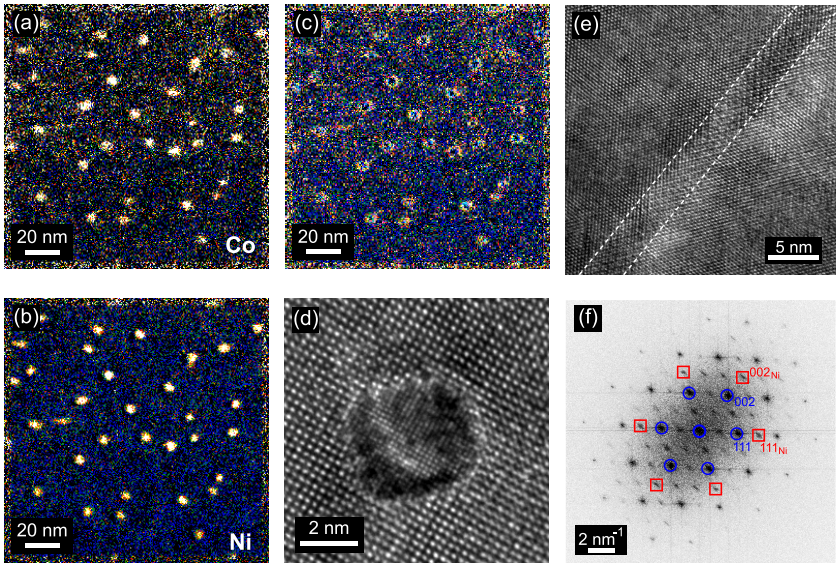

Figure 4. (a) EFTEM plane-view of a $Co_{0.32}Ni_{0.68}$ nanowires assembly embedded in $CeO_2/SrTiO_3(001)$ at the Co L-edge. Bright spots indicate a high Co concentration. (b) EFTEM plane-view of $Co_{0.32}Ni_{0.68}$ nanowires assembly embedded in $CeO_2/SrTiO_3(001)$ at the Ni L-edge. Bright spots indicate a high Ni concentration. (c) Digital difference of images in panels a and b evidencing the fact that Co and Ni are located within the same areas. (d) High resolution TEM plane view of an epitaxial $Co_{0.32}Ni_{0.68}$ nanowire in $CeO_2/SrTiO_3(001)$. (e) High resolution TEM cross section of an epitaxial $Co_{0.32}Ni_{0.68}$ nanowire in $CeO_2/SrTiO_3(001)$. (f) Fourier transform of panel e with indexed spots assuming cube-on-cube epitaxy of the cubic alloy and the matrix.

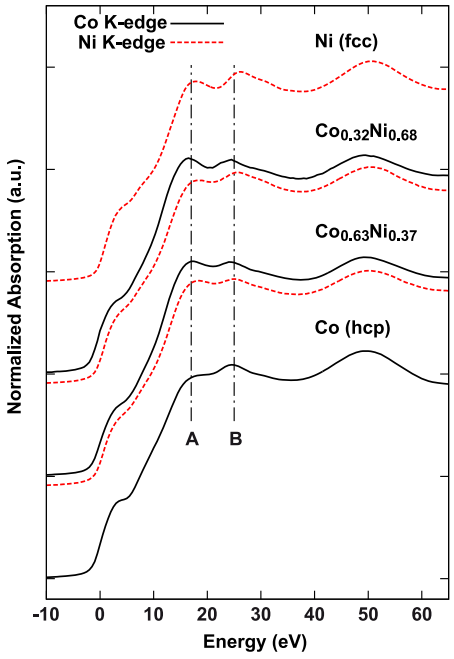

Figure 5. XANES spectra recorded at the Co (continuous line) and Ni (dashed line) K edges. Co and Ni spectra have been aligned in energy for comparison; spectra of pure Ni (fcc) and Co (hcp) metal foils are shown as top and bottom curves, respectively. Spectra of $Co_{0.32}Ni_{0.68}$ and $Co_{0.63}Ni_{0.37}$ exhibit a ratio of A and B peaks intensities corresponding to a fcc structure at both Co and Ni edges.

storage density of 1 Tbit·in.$^{-2}$ required for high density storage media.

Having established the combinatorial approach as a way to obtain self-assembled Co_xNi_{1-x} alloy nanowires, we now examine the magnetic properties of these systems. Figure 6 shows magnetization loops obtained for pure Ni nanowires (a) and $Co_{0.63}Ni_{0.37}$ nanowires (b), recorded with the field applied along the wires axis (out of plane direction) and perpendicular (in plane). The Ni wires assembly exhibits an unexpected behavior: the two magnetization loops are almost identical, indicating that the magnetic anisotropy of the system is very weak. This is at variance with the most commonly observed situation in magnetic nanowires assemblies: a large magnetic anisotropy dominated by shape anisotropy, with an easy axis along the wires axis and a hard plane perpendicular to this axis. Such a response is recovered for the Co_xNi_{1-x} alloy nanowires: with the field applied along the wires axis, the magnetization loop is open with remanence magnetization (M_r) and coercive field (H_c) much larger than with the field applied in plane.

Analysis of the strain in Ni nanowires from X-ray diffraction data reveals a tensile strain ε along the [001] direction (parallel to the axis). In contrast, no strain could be detected in the (001) plane. The uniaxial deformation of the wires leads to a large magnetoelastic anisotropy, given by $K_{me} = 3/2\lambda_{001}(c_{11} - c_{12})\varepsilon$, where λ_{001} is the magnetostrictive parameter along [001] and c_{ij} are elastic coefficients. As $K_{me} < 0$ in pure Ni, this contribution competes with the magnetostatic anisotropy K_m. Both contributions being of the same order of magnitude, $K_m + K_{me} \approx 0$ and the residual anisotropy is quite small in Ni nanowires assemblies. A complete analysis of the strain and magnetic anisotropy in Ni nanowires is outside the scope of the present

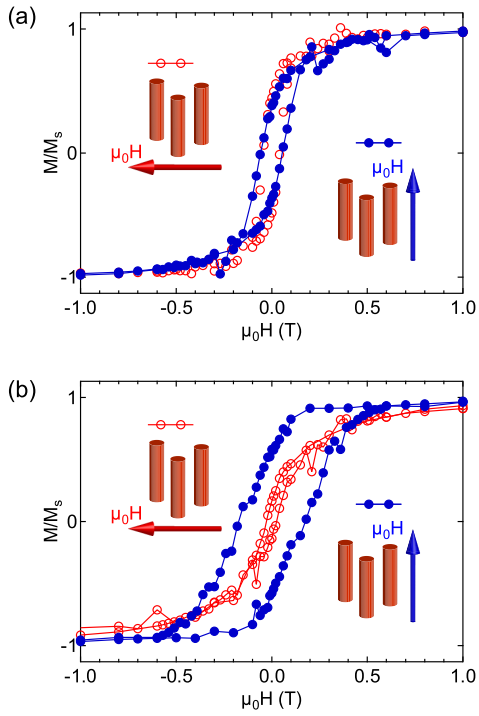

Figure 6. (a) Magnetic hysteresis cycles at 10 K with field parallel (disks) and perpendicular (circles) to the wires obtained for a Ni nanowires assembly embedded in CeO_2/$SrTiO_3$(001). (b) Magnetic hysteresis cycles at 10 K with field parallel (disks) and perpendicular (circles) to the wires obtained for a $Co_{0.63}Ni_{0.37}$ nanowires assembly embedded in CeO_2/$SrTiO_3$(001).

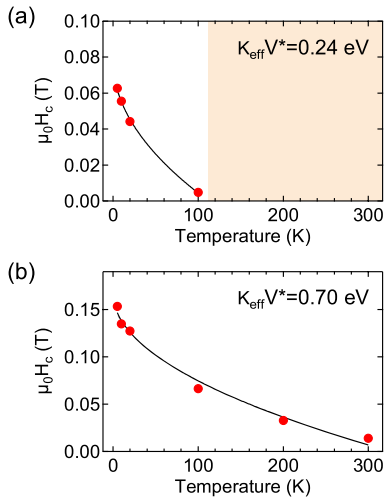

Figure 7. (a and b) Coercive field as a function of the temperature for Ni nanowires (a) and $Co_{0.63}Ni_{0.37}$ nanowires (b). The line is a fit to the Sharrock's formula, as described in the text. The shaded area in panel a corresponds to the superparamagnetic regime.

paper and will be published elsewhere. The fact that the magnetic anisotropy is very weak in Ni nanowires embedded in CeO_2/$SrTiO_3$(001) epilayers makes such a system an ideal starting point for designing systems with tailored magnetic properties by Co alloying. Indeed, such engineering of the magnetic anisotropy is possible because both the saturation magnetization, M_s, and the magnetostrictive parameter λ_{001} depend on the Co content in Co_xNi_{1-x} alloys.[21,22] M_s increases with the Co content and so does K_m that is proportional to M_s^2. Starting from negative values, λ_{001} also increases with the Co content and even changes sign beyond $x = 0.1$. Thus, increasing the Co content should lead to an overall increase of the total magnetic anisotropy of the system.

This enhancement of the magnetic anisotropy with increasing Co content is exactly what is observed, as shown by the strikingly dissimilar loops in Figure 6a,b. It is also reflected by the drastically distinct evolutions of the coercive field, μ_0H_c, of pure Ni wires and alloy wires with the temperature. μ_0H_c decreases sharply with the temperature in Ni nanowires, Figure 7a. Beyond 100 K, $\mu_0H_c = 0$, indicating that the system has entered the superparamagnetic regime: the energy barrier linked to magnetic anisotropy is not sufficiently large compared to thermal energy to ensure the stability of the magnetization in a given direction. The value of this energy barrier, $K_{eff}V^*$ with K_{eff} the effective anisotropy of the system and V^* the activation volume, can be deduced by fitting $\mu_0H_c(T)$ using Sharrock's formula:[23] $\mu_0H_c(T) = \mu_0H_{c,0}[1 - (25k_BT/K_{eff}V^*)^{1/2}]$, where $\mu_0H_{c,0}$ is the coercive field at $T = 0$ K and k_B is the Boltzmann constant. In the case of Ni wires, we get a barrier of 0.24 eV.

Such a transition toward the superparamagnetic regime at temperatures below 300 K is not observed in the case of alloys nanowires. Although μ_0H_c decreases with T, see Figure 7b, it remains positive at room temperature. The ferromagnetic state is thus preserved at 300 K, as attested by the magnetic cycles in Figure 8a,b. This is a direct consequence of the increase of the magnetic anisotropy. Indeed, analysis of $\mu_0H_c(T)$ data yields a value of 0.70 eV for the energy barrier of $Co_{0.63}Ni_{0.37}$ nanowires, to be compared with the much smaller value found in Ni.

The magnetic loops taken in the hard direction do not evolve drastically when the temperature increases, Figure 8a, and the anisotropy is still quite pronounced at 300 K as shown in Figure 8b. Comparison of the magnetic cycles of $Co_{0.32}Ni_{0.68}$ and $Co_{0.63}Ni_{0.37}$ nanowires assemblies reveals that the anisotropy is stronger when the Co content increases: along the hard direction, the saturation field is larger in $Co_{0.63}Ni_{0.37}$ as shown in Figure 8c. The increase of the Co content also leads to a less pronounced variation of the saturation magnetization with the temperature, Figure 8d.

Going further, K_{eff} can be evaluated by exploiting the magnetometry data: $K_{eff} = 1/2(\mu_0M_s\Delta H_s)$, where ΔH_s is the difference of the saturation fields perpendicular to the wires axis and parallel to it.[24,25] Applying such procedure, we get $K_{eff} = 1.2 \times 10^5$ J/m^3 for the $Co_{0.38}Ni_{0.62}$ nanowires assembly and $K_{eff} = 3.7 \times 10^5$ J/m^3 for $Co_{0.63}Ni_{0.37}$ at 10 K. K_{eff} can be compared to the magnetostatic part of the magnetic anisotropy

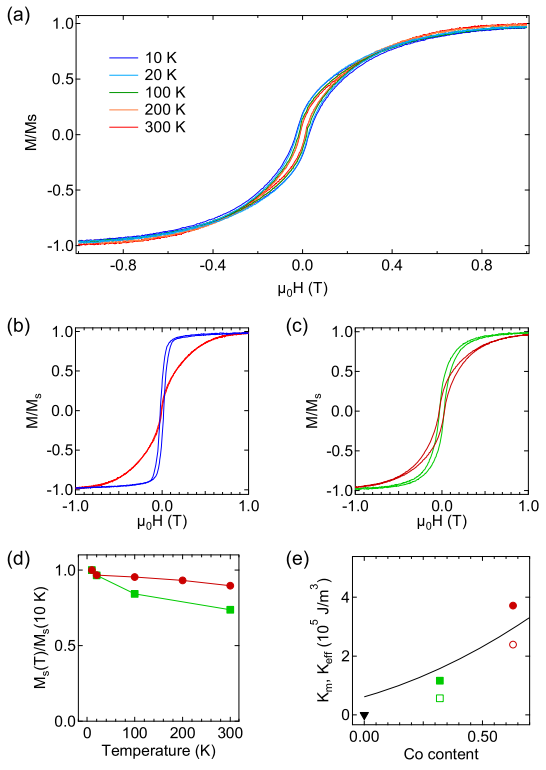

Figure 8. (a) Magnetic hysteresis cycles at 10, 20, 100, 200, and 300 K with field applied perpendicular to the wires obtained for a $Co_{0.63}Ni_{0.37}$ nanowires assembly embedded in $CeO_2/SrTiO_3$(001). (b) Magnetic hysteresis cycles at 300 K with field parallel (blue line) and perpendicular (red line) to the wires obtained for a $Co_{0.63}Ni_{0.37}$ nanowires assembly embedded in $CeO_2/SrTiO_3$(001). (c) Magnetic hysteresis cycles at 10 K with field applied perpendicular to the wires obtained for $Co_{0.32}Ni_{0.68}$ (green line) and $Co_{0.63}Ni_{0.37}$ (dark red line) nanowires assemblies. (d) Magnetization as a function of the temperature of $Co_{0.32}Ni_{0.68}$ (squares and green line) and $Co_{0.63}Ni_{0.37}$ (disks and dark red line) nanowires assemblies. (e) Black line: Magnetostatic anisotropy, K_m, at low temperature as a function of the Co content. Black triangle: magnetic anisotropy of Ni wires. K_{eff}, magnetic anisotropy extracted from magnetometry, of $Co_{0.32}Ni_{0.68}$ (green plain square, T = 10 K; open square, T = 300 K) and $Co_{0.63}Ni_{0.37}$ (dark red disk, T = 10 K; circle, T = 300 K) nanowires assemblies.

(shape anisotropy and dipolar interwire coupling) that is given by: $K_m = 1/4(\mu_0 M_s^2)(1 - 3P)$, where P is the volume fraction occupied by the wires.[26] The results are summarized in Figure 8e, where values of the anisotropy are given at 10 and 300 K. The fact that K_{eff} is smaller at 300 K than at 10 K is related to the drop of M_s with increasing T. The results indicate that K_{eff} increases with the Co content and reaches values approaching K_m for $x = 0.63$.

To conclude on the magnetic properties, increasing the Co content in the alloy nanowires leads to a substantial increase of the magnetic anisotropy. As a consequence, the transition to the superparamagnetic regime occurs at temperatures exceeding room temperature. Also, the drop in saturation magnetization with increasing temperature is largely suppressed for $x = 0.63$.

We close this section by underlining the fact that the combinatorial approach for the growth of alloys nanowires proposed here may be generalized to other materials. In the field of magnetic nanowires, soft $Ni_{1-x}Fe_x$ and hard $Co_{1-x}Pt_x$ alloys may be grown. The method is not restricted to the growth of ferromagnetic nanowires and could be generalized to other couples of materials, with distinct properties. A recent study showed the relevance of $BaTiO_3/CeO_2$ nanocomposites in order to obtain materials with tunable dielectric and ferroelectric properties.[27] Using the combinatorial approach would allow to add another degree of freedom in the optimization of the composite by tuning the composition x of $Ba_{1-x}Sr_xTiO_3/CeO_2$ nanocomposites. Likewise, alloying may be used in order to tune the ferroelectric response in composites made of a ferroelectric compound and another material. Other original issues may be explored, such as the growth of nanowires with concentration gradient along their axis.

CONCLUSIONS

In the present paper, we have demonstrated the use of combinatorial schemes in order to grow self-assembled vertical epitaxial *alloy* nanostructures. This has been demonstrated in the case of Co_xNi_{1-x} alloy nanowires embedded in $CeO_2/SrTiO_3$(001) epilayers. Furthermore, we provide an illustration of the advantages offered by the combinatorial approach that can be used to engineer a physical property: in the case of Co_xNi_{1-x} wires, we show that the magnetic anisotropy of the system can be tuned by controlling the Co content, a parameter that can be adjusted at will using the combinatorial approach. To conclude, we would like to stress that the growth of alloy nanostructures is one of the perspectives offered by the growth technique employed here. Other promising issues may be explored in a near future. Indeed, by adjusting the growth sequences, it should be possible to grow axially structured nanostructures with, *e.g.*, composition or diameter axial modulation. This would pave the way towards real three-dimensional self-assembly of monolithic embedded epitaxial nanostructures.

METHODS

Sample Growth. The growth method used relies on sequential pulsed laser deposition (PLD) of Ni and CeO_2 in reductive conditions ($P_{growth} \leq 10^{-5}$ mbar). The epilayers were grown on $SrTiO_3$(001) substrates using a quadrupled Nd:YAG laser (wavelength 266 nm) operating at 10 Hz and a fluence in the 1−3 J·cm^{-2} range. CoO, NiO and CeO_2 targets were used. Tuning the ratio of laser shots on the two targets enabled us to

modify the Ni and Co content in the epilayers. Prior to the growth of the nanowires assembly, a 4 nm thick pure CeO_2 epilayer was deposited on $SrTiO_3(001)$ at 650 °C and 10^{-2} mbar of oxygen. This step ensures the subsequent epitaxial growth of the CeO_2 matrix under vacuum, with the following epitaxial relationship: $(001)_f/(001)_s$, $[110]_f \| [100]_s$, $[1\bar{1}0]_f \| [010]_s$, where *s* and *f* subscripts denote the substrate and film, respectively. After the buffer growth, the sample was kept at the same temperature and the pressure lowered to less than 10^{-5} mbar. The growth of the embedded Ni nanowires assembly was then performed using the following sequence: [30 shots on the CeO_2 target followed by 10 shots on the NiO target] repeated 800 times. The growth of embedded Co_xNi_{1-x} alloy nanowires was performed using the [6 shots on the CeO_2 target, 2 shots on the NiO target, 6 shots on the CeO_2, 1 shot on the CoO target] sequence (S1) repeated 1300 times and [6 shots on the CeO_2 target, 1 shot on the NiO target, 6 shots on the CeO_2, 2 shots on the CoO target] sequence (S2) repeated 1300 times. We have thus samples with a Ni/Co nominal ratio of 2 and 1/2.

Sample Analysis. High resolution and energy-filtered transmission electron microscopy data were acquired using a JEOL JEM 2100F equipped with a field-emission gun operated at 200 kV and a Gatan GIF spectrometer. Energy dispersive X-ray spectroscopy was used to calibrate the Co and Ni percentage within the nanowires from analysis of the Co and Ni K_α peaks. Sequence (S1) led to $Co_{0.32}Ni_{0.68}$ and sequence (S2) led to $Co_{0.63}Ni_{0.37}$.

X-ray absorption spectroscopy data were collected at the Ni and Co K-edges spectra range at the SAMBA beamline of Synchrotron SOLEIL. The K_α fluorescence yields of Co and Ni were monitored by a 36 pixels monolithic Germanium detector (Canberra France). Opting for fluorescence detection allowed us to probe the whole epilayers.

X-ray diffraction data were collected on a laboratory 4-circles diffractometer (Philips X'Pert MRD) and at the SIXS beamline at synchrotron SOLEIL (proposal number 20110234). At SIXS, data were collected with 15.575 keV monochromatic radiation. The reciprocal space coordinates (*hkl*) are defined in the (*a**, *b**, *c**) basis of the reciprocal lattice of cubic $SrTiO_3$. The surface normal (growth direction) is oriented along *c**.

Magnetic measurements were performed in a superconducting quantum device (SQUID) magnetometer (Quantum Design MPMS - 5S) and a vibrating sample magnetometer (Quantum Design PPMS). The data were corrected by removing the diamagnetic contribution of the substrate (obtained by extrapolating the high-field slope), in order to keep only the ferromagnetic contribution.

Conflict of Interest: The authors declare no competing financial interest.

Acknowledgment. We are grateful to the SOLEIL staff for smoothly running the facility and to F. Breton for the design of the PLD control system. We acknowledge support from Agence Nationale de la Recherche, contract ANR-2011-BS04-007-01. This work was also supported by the Region Ile-de-France in the framework of C'Nano IdF (project Nadia). C'Nano IdF is the nanoscience competence center of Paris Region, supported by CNRS, CEA, MESR and Region Ile-de-France. We thank B. Capelle and J.-M. Guigner, IMPMC, CNRS-UPMC, for access to the TEM facilities.

REFERENCES AND NOTES

1. MacManus-Driscoll, J. L. Self-Assembled Heteroepitaxial Oxide Nanocomposite Thin Film Structures: Designing Interface-Induced Functionality in Electronic Materials. *Adv. Func. Mater.* **2010**, *20*, 2035–2045.
2. Zheng, H.; Wang, J.; Lofland, S. E.; Ma, Z.; Mohaddes-Ardabili, L.; Zhao, T.; Salamanca-Riba, L.; Shinde, S. R.; Ogale, S. B.; Bai, F.; *et al.* Multiferroic $BaTiO_3$-$CoFe_2O_4$ Nanostructures. *Science* **2004**, *303*, 661–663.
3. Mohaddes-Ardabili, L.; Zheng, H.; Ogale, S. B.; Hannoyer, B.; Tian, W.; Wang, J.; Lofland, S. E.; Shinde, S. R.; Zhao, T.; Jia, Y.; *et al.* Self-Assembled Single-Crystal Ferromagnetic Iron Nanowires Formed by Decomposition. *Nat. Mater.* **2004**, *3*, 533–538.
4. Zheng, H.; Straub, F.; Zhan, Q.; Yang, P.-L.; Hsieh, W.-K.; Zavaliche, F.; Chu, Y.-H.; Dahmen, U.; Ramesh, R. Self-Assembled Growth of $BiFeO_3$-$CoFe_2O_4$ Nanostructures. *Adv. Mater.* **2006**, *18*, 2747–2752.
5. Zheng, H.; Zhan, Q.; Zavaliche, F.; Sherburne, M.; Straub, F.; Cruz, M. P.; Chen, L.-Q.; Dahmen, U.; Ramesh, R. Controlling Self-Assembled Perovskite-Spinel Nanostructures. *Nano Lett.* **2006**, *6*, 1401–1407.
6. MacManus-Driscoll, J. L.; Zerrer, P.; Wang, H.; Yang, H.; Yoon, J.; Fouchet, A.; Yu, R.; Blamire, M. G.; Jia, Q. Strain Control and Spontaneous Phase Ordering in Vertical Nanocomposite Heteroepitaxial Thin Films. *Nat. Mater.* **2008**, *7*, 314–320.
7. Zhan, Q.; Yu, R.; Crane, S. P.; Zheng, H.; Kisielowski, C.; Ramesh, R. Structure and Interface Chemistry of Perovskite-Spinel Nanocomposite Thin Films. *Appl. Phys. Lett.* **2006**, *89*, 172902.
8. Dix, N.; Muralidharan, R.; Rebled, J.-M.; Estrade, S.; Peiro, F.; Varela, M.; Fontcuberta, J.; Sanchez, F. Selectable Spontaneous Polarization Direction and Magnetic Anisotropy in $BiFeO_3$-$CoFe_2O_4$ Epitaxial Nanostructures. *ACS Nano* **2010**, *4*, 4955–4961.
9. Chen, A.; Bi, Z.; Hazariwala, H.; Zhang, X.; Su, Q.; Chen, L.; Jia, Q.; MacManus-Driscoll, J. L.; Wang, H. Microstructure, Magnetic, and Low-Field Magnetotransport Properties of Self-Assembled $(La_{0.7}Sr_{0.3}MnO_3)(0.5)$:$(CeO_2)(0.5)$ Vertically Aligned Nanocomposite Thin Films. *Nanotechnology* **2011**, *22*, 315712.
10. Aimon, N. M.; Kim, D. H.; Choi, H. K.; Ross, C. A. Deposition of Epitaxial $BiFeO_3$/$CoFe_2O_4$ Nanocomposites on (001) $SrTiO_3$ by Combinatorial Pulsed Laser Deposition. *Appl. Phys. Lett.* **2012**, *100*, 092901.
11. Shin, J.; Goyal, A.; Cantoni, C.; Sinclair, J. W.; Thompson, J. R. Self-Assembled Ferromagnetic Cobalt/Yttria-Stabilized Zirconia Nanocomposites for Ultrahigh Density Storage Applications. *Nanotechnology* **2012**, *23*, 155602.
12. Fruchart, O.; Klaua, M.; Barthel, J.; Kirschner, J. Self-Organized Growth of Nanosized Vertical Magnetic Co Pillars on Au(111). *Phys. Rev. Lett.* **1999**, *83*, 2769–2772.
13. Liu, H.-J.; Chen, L.-Y.; He, Q.; Liang, C.-W.; Chen, Y.-Z.; Chien, Y.-S.; Hsieh, Y.-H.; Lin, S.-J.; Arenholz, E.; Luo, C.-W.; *et al.* Epitaxial Photostriction-Magnetostriction Coupled Self-Assembled Nanostructures. *ACS Nano* **2012**, *6*, 6952–6959.
14. Vidal, F.; Zheng, Y.; Milano, J.; Demaille, D.; Schio, P.; Fonda, E.; Vodungbo, B. Nanowires Formation and the Origin of Ferromagnetism in a Diluted Magnetic Oxide. *Appl. Phys. Lett.* **2009**, *95*, 152510.
15. Schio, P.; Vidal, F.; Zheng, Y.; Milano, J.; Fonda, E.; Demaille, D.; Vodungbo, B.; Varalda, J.; de Oliveira, A. J. A.; Etgens, V. H. Magnetic Response of Cobalt Nanowires With Diameter Below 5 nm. *Phys. Rev. B* **2010**, *82*, 094436.
16. Vidal, F.; Schio, P.; Keller, N.; Zheng, Y.; Demaille, D.; Bonilla, F. J.; Milano, J.; de Oliveira, A. J. A. Magneto-Optical Study of Slanted Co Nanowires Embedded in CeO_2/$SrTiO_3(001)$. *Physica B* **2012**, *407*, 3070–3073.
17. Vidal, F.; Zheng, Y.; Schio, P.; Bonilla, F. J.; Barturen, M.; Milano, J.; Demaille, D.; Fonda, E.; de Oliveira, A. J. A.; Etgens, V. H. Mechanism of Localization of the Magnetization Reversal in 3 nm Wide Co Nanowires. *Phys. Rev. Lett.* **2012**, *109*, 117205.
18. Miyawaki, J.; Matsumura, D.; Nojima, A.; Yokoyama, T.; Ohta, T. Structural Study of Co/Pd(111) and CO/Co/Pd(111) by Surface X-ray Absorption Fine Structure Spectroscopy. *Surf. Sci.* **2007**, *601*, 95–103.
19. Zhang, G. L.; Wu, Z. Y.; Li, A. G.; Wang, Y. S.; Zhang, J.; Abbas, M. I.; Hu, R.; Ni, X. B.; Tong, Y. P.; Hwu, Y. K. XANES Investigation of the Local Structure of Co Nanoclusters Embedded in Ag. *Phys. Rev. B* **2004**, *69*, 115405.
20. Castaner, R.; Prieto, C.; Deandres, A.; Martinez, J. L.; Martinez Albertos, J. L.; Ocal, C.; Miranda, R. The Structural Characterization of Co-Cu(100) Superlattices by X-ray-Absorption Spectroscopy. *J. Phys.: Condens. Matter* **1994**, *6*, 4981–4990.

21. Hall, R. C. Single Crystal Anisotropy and Magnetostriction Constants of Several Ferromagnetic Materials Including Alloys of NiFe, SiFe, AlFe, CoNi, and CoFe. *J. Appl. Phys.* **1959**, *30*, 816–819.
22. Collins, M. F.; Wheeler, D. A. Magnetic Moments and Degree of Order in Cobalt-Nickel Alloys. *Proc. Phys. Soc., London* **1963**, *82*, 633.
23. Sharrock, M. P. Time Dependence of Switching Fields in Magnetic Recording Media. *J. Appl. Phys.* **1994**, *76*, 6413.
24. Rosa, W. O.; Vivas, L. G.; Pirota, K. R.; Asenjo, A.; Vázquez, M. Influence of Aspect Ratio and Anisotropy Distribution in Ordered CoNi Nanowires Arrays. *J. Magn. Magn. Mater.* **2012**, *324*, 3679–3682.
25. Pirota, K. R.; Silva, E. L.; Zanchet, D.; Navas, D.; Vázquez, M.; Hernández-Vélez, M.; Knobel, M. Size Effect and Surface Tension Measurements in Ni and Co Nanowires. *Phys. Rev. B* **2007**, *76*, 233410.
26. Encinas-Oropesa, A.; Demand, M.; Piraux, L.; Huynen, I.; Ebels, U. Dipolar Interactions in Arrays of Nickel Nanowires Studied by Ferromagnetic Resonance. *Phys. Rev. B* **2001**, *63*, 104415.
27. Yamada, T.; Sandu, C. S.; Gureev, M.; Sherman, V. O.; Noeth, A.; Muralt, P.; Tagantsev, A. K.; Setter, N. Self-Assembled Perovskite-Fluorite Oblique Nanostructures for Adaptive (Tunable) Electronics. *Adv. Mater.* **2009**, *21*, 1363–1367.